Insights into the elastic properties of RE-*i*-MAX phases and their potential exfoliation into two-dimensional RE-*i*-MXenes

A. Champagne,[1] F. Ricci,[1] M. Barbier,[2,3] T. Ouisse,[2] D. Magnin,[1] S. Ryelandt,[4] T. Pardoen,[4] G. Hautier,[1] M. W. Barsoum,[5] and J.-C. Charlier[1]

[1]*Institute of Condensed Matter and Nanosciences, Université catholique de Louvain, B-1348 Louvain-la-Neuve, Belgium*
[2]*Univ. Grenoble Alpes, CNRS, Grenoble INP, LMGP, F-38000 Grenoble, France*
[3]*European Synchrotron Radiation Facility, CS40220, F-38043 Grenoble Cedex 9, France*
[4]*Institute of Mechanics, Materials and Civil Engineering, Université catholique de Louvain, B-1348 Louvain-la-Neuve, Belgium*
[5]*Department of Materials Science and Engineering, Drexel University, Philadelphia, Pennsylvania 19104, USA*

(Received 8 November 2019; published 13 January 2020)

The recent discovery of quaternary MAX phases with chemical in-plane order allowed the addition of non-traditional MAX phase elements, such as rare-earth elements. In the present study, first-principles calculations are performed to investigate the electronic structure, elastic and hardness response, and bonding strengths of the novel RE-*i*-MAX phases with the formula $(Mo_{2/3}RE_{1/3})_2AlC$. The Voigt-Reuss-Hill bulk, shear, and Young's moduli are compared along the series of RE = Nd, Sm, Gd, Tb, Dy, Ho, Er, Tm, and Lu, and the global trend is found to depend on the unit cell volume. Nanoindentation experiments on Ho-based single crystals result in moduli that are within 10% of predicted values and a hardness of ∼10 GPa. The computation of the projected density of states, projected crystal orbital Hamilton population, and integrated projected crystal orbital Hamilton population, reveals that the bonding of Mo and RE atoms with the Al atoms are weaker than those with the C atoms, suggesting the exfoliation of RE-*i*-MAX into two-dimensional RE-*i*-MXenes to be feasible. Such a possibility to form two-dimensional crystals is further confirmed by the computation of the exfoliation energies, which demonstrates the process to be easier as the RE atomic mass decreases.

DOI: 10.1103/PhysRevMaterials.4.013604

I. INTRODUCTION

The more than 150 ternary carbides and nitrides, with the general formula $M_{n+1}AX_n$, form a relatively new class of layered ceramics composed of two-dimensional (2D) $M_{n+1}X_n$ sheets separated by A layers, where M represents an early transition metal, A an element from groups 13 to 16, X either a carbon or a nitrogen atom, and n varies from 1 to 3 [1,2]. Beyond their unique sets of properties combining some of the best properties of metals and ceramics [1,3–7], the MAX phases have attracted growing interest for their use as parent materials to produce their 2D derivatives, MXenes [8]. The chemical exfoliation of MAX phases into 2D MXenes, first reported in 2011 [8], constitutes a major breakthrough in the synthesis of novel 2D systems, and today more than 30 MXenes, with various compositions, have been successfully obtained [9]. Thanks to their versatile chemistry and the control of surface terminations, MXenes are fast becoming one of the largest family of 2D materials competing in an impressive number of applications, including energy storage devices, sensors, conductive transparent electrodes, and electromagnetic interference shielding [10,11].

Recently, a new route to increase the elemental combination of MAX phases and to optimize their performance was proposed, consisting in the addition of a fourth element, by alloying on the M, A, or X sites [12–14]. Out-of-plane ordered (*o*-MAX) [15], and in-plane ordered (*i*-MAX) quaternary MAX phases were synthesized [16,17], and recently the existence of rare-earth (RE) containing *i*-MAX phases, coined RE-*i*-MAX, with the general formula $(M_{2/3}RE_{1/3})_2AC$, was revealed [18,19]. The $(Mo_{2/3}RE_{1/3})_2AlC$ phases were described by space group No. 15 ($C2/c$), as opposed to No. 94 ($P6_3/mmc$) for traditional MAX phases. Because of their magnetic properties [18], these new phases are expected to attract much attention from the scientific community. Moreover, since these new systems are Al based, the Al should, in principle, be selectively etched to create RE-*i*-MXenes, where the RE elements are ordered in the basal plane. This would significantly increase the palette of available magnetic 2D crystals that could be used in future 2D electronic and spintronic devices.

Motivated by these recent discoveries and by the possibility to use these magnetic phases as precursor layered compounds for synthesizing 2D magnetic MXenes, herein first-principles calculations are used to investigate the electronic and elastic properties of $(Mo_{2/3}RE_{1/3})_2AlC$ systems, with RE = Nd, Sm, Gd, Tb, Dy, Ho, Er, Tm, and Lu. We also present a complete analysis of the bond strengths within the RE-*i*-MAX family and compute the static exfoliation energies to gain insight into their exfoliation potential. Finally, a Ho-based single crystal is characterized through nanoindentation to determine its Young's modulus and hardness.

II. THEORETICAL METHODS AND EXPERIMENTAL TECHNIQUES

A. Computational methods

The structural and electronic properties of the nine $(Mo_{2/3}RE_{1/3})_2AlC$ compounds were computed *ab initio*

 ©2020 American Physical Society

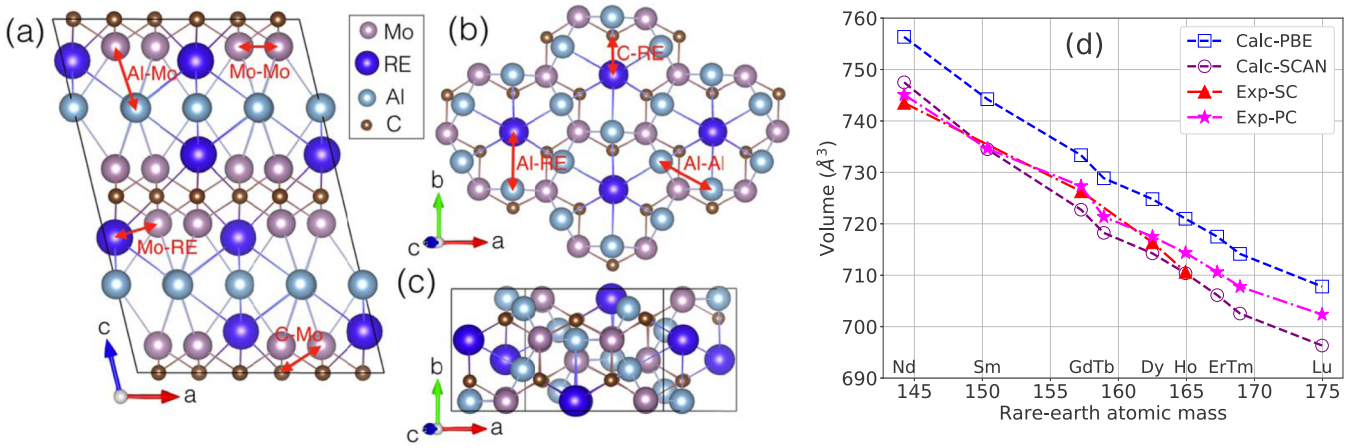

FIG. 1. Schematic representation of the conventional monoclinic $C2/c$ cell of $(Mo_{2/3}RE_{1/3})_2AlC$, RE = Nd, Sm, Gd, Tb, Dy, Ho, Er, Tm, or Lu, along the (a) [010], and (b) and (c) [103] zone axes. Some specific interatomic bonds are defined with red arrows. RE, Mo, Al, and C atoms are represented by dark blue, purple, light blue, and brown spheres, respectively. (d) Dependence of the conventional cell volume on rare-earth atomic mass, computed with both GGA-PBE (squares: blue dashed line) and SCAN functionals (circles: violet dashed line), compared to experimental volumes extracted from Refs. [18,30] for (SC) single crystals (triangles: red dotted dashed line) and (PC) polycrystals (stars: pink dotted dashed line), respectively.

using density functional theory (DFT) [20,21] as implemented in the Vienna *ab initio* simulation package (VASP) [22–24]. The exchange-correlation functional was approximated in two ways. In the first we used the Perdew-Burke-Ernzerhof generalized gradient approximation (PBE-GGA), [25] and in the second we used the strongly constrained and appropriately normed (SCAN) meta-GGA approximation, recently introduced by Sun *et al.* [26,27]. Projector augmented wave (PAW) pseudopotentials [28,29] were used, with the $4f$ electrons of the RE elements frozen in the core. Following previous works on RE-containing MAX phases [17,18,30], the non-spin-polarized approach was considered. A plane wave kinetic energy cutoff of 520 eV was used. The first Brillouin zone was sampled with a $11 \times 11 \times 4$ Monkhorst-Pack k-point grid [31] and a Gaussian smearing of 0.2 eV was used to accelerate the convergence. For all systems, the unit cell parameters and the atomic positions were fully optimized until the largest force was smaller than 0.1 meV/Å. The electronic density of states (DOS) and the projected crystal orbital Hamilton population (pCOHP) of each system were computed using the local orbital basis suite towards electronic structure reconstruction (LOBSTER) code [32–34], with the pbeVaspFit2015 basis set [35]. This COHP technique allows us to partition the electronic band structure into bonding, nonbonding, and antibonding contributions of the localized atomic basis sets and also provides information about the bonding strengths.

Additionally, the 6×6 single crystal elastic tensor of each system was determined by applying a set of homogeneous finite deformations of the lattice and calculating the associated resulting stress, as implemented in the VASP code [22–24]. The elastic constants C_{ij} were derived from the strain-stress relationship $\sigma_i = \sum_{j=1-6} C_{ij}\varepsilon_j$, where σ_i corresponds to a small stress component resulting from the application of a small strain ε_j to the relaxed system [36]. Eventually, exfoliation energies of RE-i-MAX phases into 2D RE-i-MXenes were computed from the ground-state energies of each compound. All atomic models were rendered using VESTA [37].

B. Elastic and hardness measurements

Single crystalline flakes of $(Mo_{2/3}Ho_{1/3})_2AlC$ were grown using a high-temperature solution growth process described in Ref. [30]. The largest platelet areas were around 3 mm^2 with thickness up to 100 μm.

The Young's modulus and hardness values of a $(Mo_{2/3}Ho_{1/3})_2AlC$ single crystal, previously fixed with superglue on an aluminum puck, were measured by a nanoindenter with a Berkovich tip and the continuous stiffness measurement mode. The indentation depth limit was set to 1 μm, with a strain rate of 0.05 s^{-1}. In total, 15 indents with a spacing of 30 μm between them were performed.

The indents resulting from the nanoindentation were imaged using a field emission gun-scanning electron microscope (JEOL 7600F) at an accelerating voltage of 15 kV and with a working distance around 12 mm. Before imaging, the samples were coated with an 8 nm gold layer using a Cressington sputter 208HR.

III. RESULTS AND DISCUSSION

A. Structural properties

As noted above, $(Mo_{2/3}RE_{1/3})_2AlC$ phases crystallize in a monoclinic $C2/c$ structure [Figs. 1(a)–1(c)] [18], like the isostructural $(M'_{2/3}M''_{1/3})_2AlC$ i-MAX phases [38]. The conventional cell includes 48 atoms—16 Mo, 8 RE, i.e., Nd, Sm, Gd, Tb, Dy, Ho, Er, Tm, or Lu, 12 Al, and 12 C atoms. The nonequivalent atomic positions are distributed in specific Wyckoff positions: $8f$ (two Mo, one RE, one Al, and one C), $4e$ (one Al), and $4d$ (one C). The theoretically predicted lattice parameters of the optimized monoclinic structures are listed in Table I and compared to previously reported experimental parameters of both monocrystalline [30] and polycrystalline samples [18]. As discussed in Ref. [30], the increase of the RE atomic mass leads to reduced lattice parameters, as expected from the decrease of the covalent atomic radius when moving

TABLE I. Structural parameters of the RE-*i*-MAX phases computed with both GGA-PBE and meta-GGA SCAN functionals considering a monoclinic $C2/c$ symmetry ($\alpha = \gamma = 90^\circ$), and compared to experimental parameters reported for single crystals (SC) [30] and polycrystals (PC) [18].

Compounds	(aÅ)	(bÅ)	(cÅ)	β(deg)	(VÅ^3)	Description
$(Mo_{2/3}Nd_{1/3})_2AlC$	9.69	5.61	14.31	103.48	756.35	Calc. PBE
	9.67	5.59	14.21	103.54	747.51	Calc. SCAN
	9.66	5.59	14.16	103.47	743.51	Expt. SC
	9.67	5.59	14.17	103.48	745.11	Expt. PC
$(Mo_{2/3}Sm_{1/3})_2AlC$	9.64	5.58	14.25	103.54	744.23	Calc. PBE
	9.61	5.56	14.15	103.61	734.51	Calc. SCAN
	9.62	5.56	14.12	103.52	734.61	Expt. PC
$(Mo_{2/3}Gd_{1/3})_2AlC$	9.59	5.55	14.18	103.58	733.34	Calc. PBE
	9.55	5.53	14.08	103.64	722.74	Calc. SCAN
	9.57	5.54	14.09	103.53	726.31	Expt. SC
	9.58	5.54	14.09	103.53	727.34	Expt. PC
$(Mo_{2/3}Tb_{1/3})_2AlC$	9.57	5.54	14.16	103.59	728.86	Calc. PBE
	9.53	5.52	14.06	103.63	718.18	Calc. SCAN
	9.55	5.52	14.07	103.54	721.36	Expt. PC
$(Mo_{2/3}Dy_{1/3})_2AlC$	9.55	5.53	14.13	103.60	724.80	Calc. PBE
	9.51	5.51	14.03	103.63	714.25	Calc. SCAN
	9.52	5.51	14.04	103.56	716.38	Expt. SC
	9.53	5.51	14.05	103.54	717.51	Expt. PC
$(Mo_{2/3}Ho_{1/3})_2AlC$	9.53	5.52	14.11	103.60	720.98	Calc. PBE
	9.49	5.49	14.01	103.62	710.38	Calc. SCAN
	9.49	5.50	14.02	103.56	710.66	Expt. SC
	9.51	5.50	14.04	103.54	714.37	Expt. PC
$(Mo_{2/3}Er_{1/3})_2AlC$	9.51	5.51	14.09	103.61	717.50	Calc. PBE
	9.47	5.48	13.99	103.61	706.13	Calc. SCAN
	9.49	5.49	14.02	103.53	710.62	Expt. PC
$(Mo_{2/3}Tm_{1/3})_2AlC$	9.40	5.50	14.07	103.61	714.15	Calc. PBE
	9.45	5.47	13.98	103.61	702.55	Calc. SCAN
	9.48	5.49	14.00	103.51	707.77	Expt. PC
$(Mo_{2/3}Lu_{1/3})_2AlC$	9.46	5.48	14.04	103.60	707.80	Calc. PBE
	9.42	5.46	13.94	103.59	696.33	Calc. SCAN
	9.45	5.47	13.97	103.48	702.36	Expt. PC

from left to right on the lanthanide row. From the values listed in Table I and plotted in Fig. 1(d), the agreement between the theoretical and experimental parameters is good, and is further improved by switching from the GGA-PBE to the SCAN functional. The SCAN functional is particularly suited to accurately compute layered materials properties [27]. Therefore, the electronic and elastic properties presented in the following sections are calculated using the SCAN functional.

B. Elastic properties

1. First-principles calculations

The elastic constants of a crystalline solid are important parameters providing information on its stiffness, stability, and anisotropy. They provide a fundamental insight into the nature of the forces acting in the material and can be seen as a link between a material's dynamical behavior and its mechanical and thermal properties. For monoclinic crystals, 13 nonzero independent elastic constants C_{ij} are defined, namely C_{11}, C_{12}, C_{13}, C_{15}, C_{22}, C_{23}, C_{25}, C_{33}, C_{35}, C_{44}, C_{46}, C_{55}, and C_{66} [39]. The single crystal elastic constants can be determined from the computation of the stress associated with a set of imposed homogeneous finite deformations. Table II lists the elastic constants C_{ij} of the $(Mo_{2/3}RE_{1/3})_2AlC$ quaternaries calculated at zero pressure and zero temperature. All RE-*i*-MAX phases considered herein fulfill the mechanical stability criteria for monoclinic crystals [40]. Moreover, in all cases, it is observed that the diagonal C_{11}, C_{22}, and C_{33} values are larger than all other constants. While for the first five systems with RE = Nd, Sm, Gd, Tb, or Dy, the principal elastic constants are classified as $C_{33} < C_{11} < C_{22}$, $(Mo_{2/3}Ho_{1/3})_2AlC$ is the only one with $C_{11} < C_{33} < C_{22}$, and the last three $(Mo_{2/3}RE_{1/3})_2AlC$ systems with RE = Er, Tm, or Lu, exhibit $C_{11} < C_{22} < C_{33}$.

From the calculated C_{ij} values, the homogenized polycrystalline elastic properties including the bulk modulus B, shear modulus G, Young's modulus E, and Poisson's ratio are computed. For monoclinic systems, the Voigt bulk and shear moduli (upper bound) can be obtained, respectively, assuming [39]

$$B_V = \tfrac{1}{9}(C_{11} + C_{22} + C_{33}) + \tfrac{2}{9}(C_{12} + C_{13} + C_{23}), \quad (1)$$

$$G_V = \tfrac{1}{15}[(C_{11} + C_{22} + C_{33}) - (C_{12} + C_{13} + C_{23}) + 3(C_{44} + C_{55} + C_{66})], \quad (2)$$

TABLE II. Calculated elastic constants C_{ij} and Voigt (V), Reuss (R), and VRH moduli (in GPa) of RE-*i*-MAX.

	Nd	Sm	Gd	Tb	Dy	Ho	Er	Tm	Lu
C_{11}	262.09	274.09	278.28	280.40	282.16	283.20	282.68	284.41	287.62
C_{12}	86.71	86.83	88.88	90.82	92.05	92.71	91.75	94.09	90.61
C_{13}	97.29	102.18	106.56	109.45	112.01	113.49	114.44	117.86	117.99
C_{15}	1.44	2.57	5.03	5.44	5.72	6.19	6.23	6.03	8.04
C_{22}	270.89	280.62	283.61	286.27	288.97	290.23	290.10	291.77	293.08
C_{23}	98.22	102.54	105.16	107.40	109.75	111.35	112.76	115.74	115.32
C_{25}	0.55	2.23	5.18	6.18	6.53	6.54	5.96	5.81	7.10
C_{33}	223.79	249.04	266.05	274.26	280.79	286.21	291.25	297.15	300.23
C_{35}	−13.41	−10.21	−6.05	−4.46	−3.93	−3.79	−4.16	−3.23	−1.66
C_{44}	96.06	99.39	101.22	102.04	102.92	103.52	104.02	103.94	104.05
C_{46}	−0.48	−0.54	−1.16	−1.49	−1.59	−1.45	−1.24	−1.26	−0.44
C_{55}	86.29	90.42	92.52	93.04	93.93	94.58	95.57	95.51	95.06
C_{66}	97.83	102.01	103.35	103.83	104.37	104.80	105.16	105.11	106.38
B_V	146.79	154.10	158.79	161.81	164.39	166.08	166.88	169.86	169.86
B_R	145.96	153.93	158.73	161.66	164.15	165.74	166.40	169.24	168.99
B_{VHR}	146.37	154.02	158.76	161.73	164.27	165.91	166.64	169.55	169.42
G_V	87.67	92.51	94.57	95.33	96.12	96.72	97.29	97.29	98.23
G_R	85.27	90.84	93.20	94.03	94.84	95.47	96.08	96.11	97.03
G_{VRH}	86.47	91.67	93.89	94.68	95.48	96.10	96.68	96.70	97.63
ν	0.25	0.25	0.25	0.26	0.26	0.26	0.26	0.26	0.26
E_{VRH}	216.73	229.49	235.28	237.66	239.95	241.64	243.05	243.76	245.70
E_1	262.09	274.09	278.28	280.40	282.16	283.20	282.68	284.41	287.62
E_2	270.81	280.62	283.61	286.27	288.97	290.23	290.10	291.77	293.08
E_3	217.20	243.98	263.79	272.93	279.69	284.96	289.45	295.85	299.99

while the Reuss bulk and shear moduli (lower bound) are given, respectively, by [39]

$$B_R = \frac{1}{(s_{11}+s_{22}+s_{33})+2(s_{12}+s_{13}+s_{23})}, \tag{3}$$

$$G_R = \frac{15}{4(s_{11}+s_{22}+s_{33})-4(s_{12}+s_{13}+s_{23})+3(s_{44}+s_{55}+s_{66})}, \tag{4}$$

where the s_{ij}'s are compliance constants obtained by inverting the 6×6 elastic constant matrix. The arithmetic averages of Voigt and Reuss moduli are known as the Hill moduli given by [41]

$$B_{VRH} = \frac{B_V + B_R}{2}, \tag{5}$$

$$G_{VRH} = \frac{G_V + G_R}{2}. \tag{6}$$

In contrast with the results reported by Dahlqvist *et al.* for $(W_{2/3}Sc_{1/3})_2AlC$ and $(W_{2/3}Y_{1/3})_2AlC$ *i*-MAX systems [42], it is noted here that the Voigt and Reuss approximations give similar values of both bulk and shear moduli (see Table II). Consequently, the Hill averages are close to these two limits. Using the calculated values of B_{VRH} and G_{VRH}, the average Young's modulus E_{VRH}, measuring the response under uniaxial tension conditions averaged over all directions, and the Poisson ratio ν, providing information about the bonding forces and reflecting the stability of a material against shear, can be obtained, respectively, assuming [41]

$$E_{VRH} = \frac{9B_{VRH}G_{VRH}}{3B_{VRH}+G_{VRH}}, \tag{7}$$

$$\nu = \frac{3B_{VRH}-2G_{VRH}}{2(3B_{VRH}+G_{VRH})}. \tag{8}$$

The values of the elastic properties reported in Table II and presented in Fig. 2 suggest that an increase of the rare-earth atomic mass, when moving from left to right on

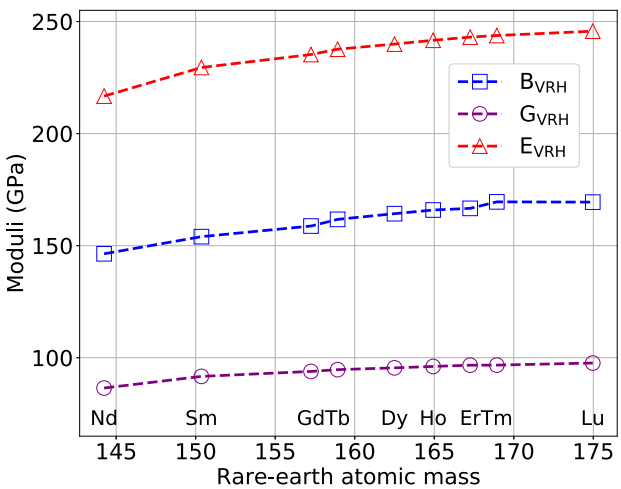

FIG. 2. Bulk (B), shear (G), and Young's (E) moduli in the Voigt-Reuss-Hill approximation, as a function of the rare-earth atomic mass.

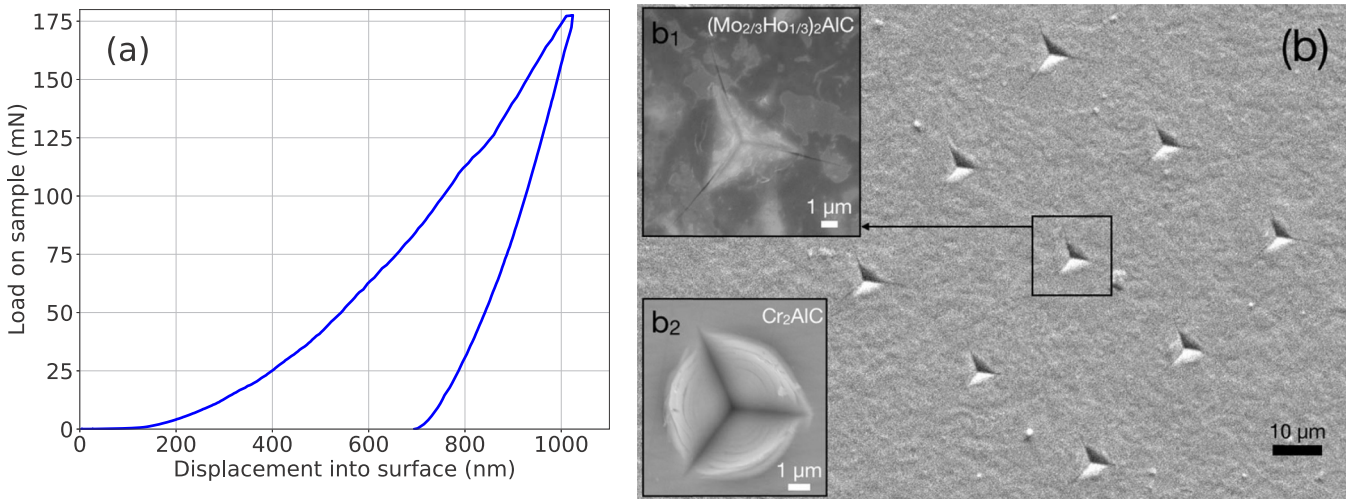

FIG. 3. (a) Representative load-displacement curve from the nanoindentation of the top surface of a Ho-based single crystal, and (b) a scanning electron microscope image of the indentation marks, with a zoom on one of these indents in inset b_1 (top left). Inset b_2 (bottom left) corresponds to a SEM image of an indent performed on a Cr_2AlC single crystal for comparison.

the lanthanide row, results in an increase of all elastic moduli. In other words, RE-*i*-MAX phases with heavier RE elements are stiffer, which is not too surprising since the unit cell, and hence the atomic bonds, tend to shrink with increasing RE atomic mass. This is consistent with the bonding strength analysis described in Ref. [30], and with the basic idea that shorter bonds are stiffer. Additionally, from Table II, the value of the Poisson ratio of all RE-*i*-MAX phases is almost constant at ∼0.26. Since the obtained values fall in the range of 0.25–0.5, it is reasonable to assume that the interatomic forces can be considered as central forces [43].

Other properties computed in this work are the directional elastic moduli

$$\frac{1}{E_i} = s_{11}l_1^4 + 2s_{12}l_1^2l_2^2 + s_{22}l_2^4 + 2s_{23}l_2^2l_3^2 + s_{33}l_3^4 + 2s_{13}l_1^2l_3^2 + s_{44}l_2^2l_3^2 + s_{55}l_1^2l_3^2 + s_{66}l_1^2l_2^2, \quad (9)$$

where l_1, l_2, and l_3 are the directional cosines of angles between the three principal directions (x, y, and z) [44]. The E_i's are very close to each other showing limited anisotropy.

2. Nanoindentation

To the authors' knowledge, this is the first time elastic properties of RE-*i*-MAX phases are reported. Therefore, in order to evaluate the accuracy of the present theoretical data, the mechanical response of a $(Mo_{2/3}Ho_{1/3})_2AlC$ single crystal was measured experimentally using nanoindentation.

A Berkovich tip is used to indent the surface of a Ho-based single crystal, perpendicularly to its *ab* plane. Fifteen indents are performed and a representative load-displacement curve is depicted in Fig. 3(a). A load of 175 mN is required to indent the sample 1 μm. A typical SEM micrograph of an indent made on $(Mo_{2/3}Ho_{1/3})_2AlC$ is shown in Fig. 3(b). Consistent with the brittle character of RE-*i*-MAX phases, small cracks are observed from the corners of the indentations, with an emanated crack length of ∼7 μm. From this point of view, RE-*i*-MAX phases differ from conventional M_2AlC phases, where the indentation induces delaminations, kinking, grain pushouts and pullouts [45], and only short cracks confined to the indenter imprint [see inset b_2 in Fig. 3(b)].

Using the Oliver and Pharr method [46,47], we calculated the average value of E_{Br} from the 15 indents to be 220 ± 8 GPa. In comparison, the computed value of the isotropic Young's modulus of $(Mo_{2/3}Ho_{1/3})_2AlC$ is 242 GPa. Even though the indentation direction is along axis 3, indentation involves a triaxial loading mode with significant compressive stresses building up in directions 1 and 2. Hence the comparison with an average isotropic modulus is appropriate. This 10% overestimation is reasonable and is typical of DFT calculations [3], considering that both defects and temperature are not taken into account in the calculations. For conventional MAX phases, an increase of the temperature by 500 °C can result in a decrease by up to 10% of the Young's modulus [3].

Another fundamental mechanical parameter that can be determined from nanoindentation is the hardness H. Using the Oliver and Pharr method [46,47], we calculated the Berkovich hardness of $(Mo_{2/3}Ho_{1/3})_2AlC$ to be 9.8 ± 0.4 GPa. In comparison, the Vickers hardness values of polycrystalline MAX phases range from 2 to 8 GPa [45].

C. Electronic structure and bonding analysis

Information on the electronic properties can be obtained from the computation of the electronic band structure and density of states (DOS). In Fig. 4, and similar to all conventional MAX and *i*-MAX phases [3,48], the RE-*i*-MAX systems exhibit a metallic behavior mostly ensured by the presence of Mo-*d* orbitals at the Fermi level. In addition, the projected COHP (pCOHP), and integrated pCOHP (IpCOHP) presented in Fig. 5, can be used to shed light on the nature of the bonding. In the present calculations, only the nearest-neighbor interactions are considered: C-Mo, C-RE, Al-Mo, Al-RE, Al-Al, Mo-Mo, and Mo-RE, as depicted in Figs. 1(a) and 1(b). Given the similarities between the nine studied systems, both Figs. 4 and 5 corresponding to the Dy-based system can be taken as references.

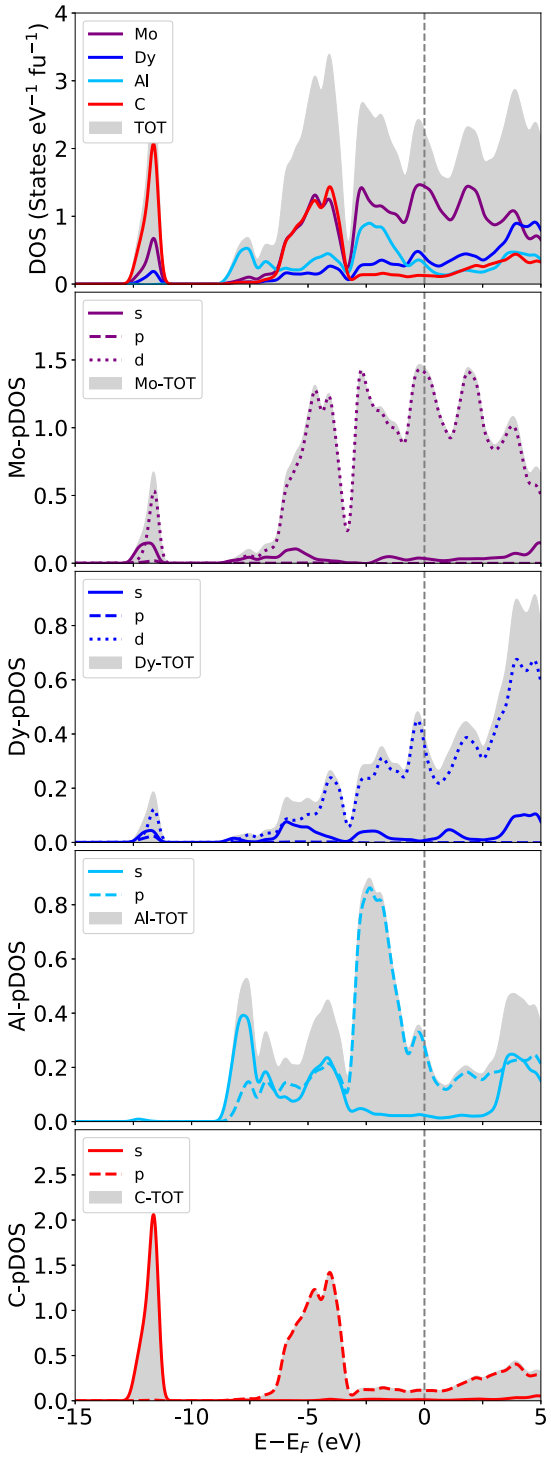

FIG. 4. Calculated electronic density of states of $(Mo_{2/3}Dy_{1/3})_2AlC$ and projected density of states on the atomic orbitals of each element, expressed in states/eV per formula unit.

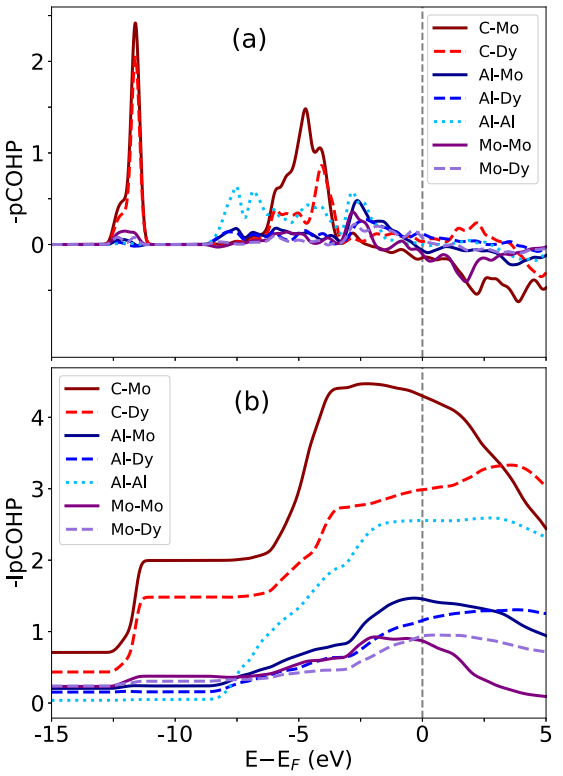

FIG. 5. Calculated (a) projected crystal orbital Hamilton population (pCOHP) and (b) integrated projected crystal orbital Hamilton population (IpCOHP) of $(Mo_{2/3}Dy_{1/3})_2AlC$.

When bringing atoms to close proximity, strong chemical bonds such as ionic and covalent bonds can form, from the transfer or sharing of electrons between atoms, respectively. Atoms usually take part in bonding via their partially filled valence orbitals. In the $(Mo_{2/3}RE_{1/3})_2AlC$ systems, the Mo atoms are involved in bonding through their 5*d* orbitals, the RE atoms, through their 5*d* and 4*f* orbitals, and both Al and C atoms, through their 2*s* and 2*p* orbitals, respectively. The pDOS presented in Fig. 4 highlights the overlap between the atomic orbitals of each element, while the −pCOHP presented in Fig. 5(a) explicitly gives information on the bonding types. In Fig. 4, the states between −13 and −11 eV can be regarded as bonding between the C-2*s* and Mo-4*d* or RE-5*d* orbitals. The pDOS of Al-2*s* and Al-2*p* orbitals are mainly distributed between −9 and −6.5 eV, and between −6.5 and −3 eV, respectively, corresponding to Al-Al bonding. Also, from −6.5 to −3 eV, C-2*p* orbitals overlap the *d* orbitals of both Mo and RE atoms, hence forming the C-Mo and C-RE covalent bonds. The states located between −3 and −1 eV can be assigned to bonding states between the Al-2*p* and the Mo-4*d* and RE-5*d* orbitals. Finally, the states in the vicinity of the Fermi level (from −1 eV and above) correspond mainly to Mo-4*d* and slightly to RE-5*d* orbitals. Consequently, the metallic character of all studied RE-*i*-MAX phases, characterized by a total DOS at the Fermi level of ∼2.5 states/eV per formula unit, arises from the *d* electrons. For this last region from −1 eV and above, the computed −pCOHP shown in Fig. 5(a) indicates that the *d* electrons of Mo and RE atoms can be seen as nonbonding electrons.

While the experimental process used to convert MAX phases into MXenes is quite complex, two main criteria, previously exploited by Khazaei and co-workers [49,50], can be used to evaluate their exfoliation potential: bonding strength and exfoliation energy. For the RE-*i*-MAX to be successfully etched into RE-*i*-MXenes, only the Al bonds, viz. Al-Mo and

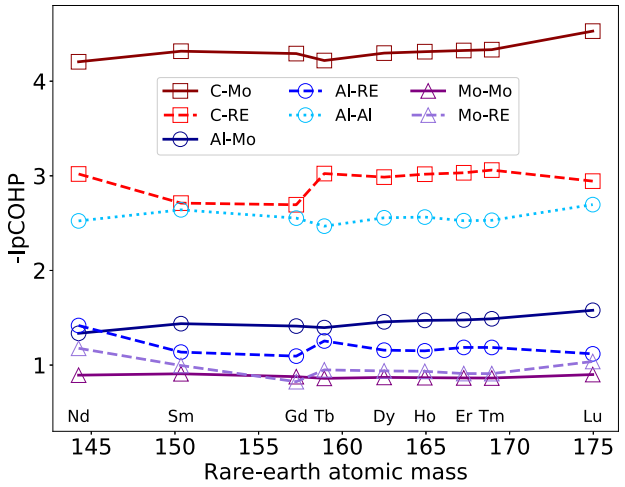

FIG. 6. −IpCOHP values at the Fermi level as a function of the rare-earth atomic mass. The relative order of bond strengths is almost unchanged with the RE atomic mass.

Al-RE, need to be broken. This would only occur if the C-Mo and C-RE bonds are stronger than the Al-Mo and Al-RE ones.

By integrating −pCOHP up to E_F, it is possible to assess the relative bonding strengths within the RE-*i*-MAX phases [32–34]. Even though no absolute value for the bond strength can be obtained, the bonds can be classified according to their −IpCOHP curve. From Figs. 5(b) and 6, the atomic interactions defined in Figs. 1(a) and 1(b) are ranked as follows: C-Mo > C-RE > Al-Al > Al-Mo > Al-RE > Mo-Mo ≈ Mo-RE. This classification is consistent with the one for conventional MAX phases, where the M-X bonds are stronger than M-A bonds [51], and presumably indicates the exfoliation potential of RE-*i*-MAX phases. Recently, Dahlqvist *et al.* reported a similar theoretical investigation about the bonding strengths within the $(W_{2/3}Y_{1/3})_2AlC$ system [42], where they concluded that C-W > Al-Al > C-Y > Al-W ≈ Al-Y. The etching of the latter resulted in $W_{1.33}C$ with ordered divacancies [38]. Consequently, the fact that C-RE bonds are strictly stronger than Al-Al ones in the RE-*i*-MAX systems investigated here may prevent the dissolution of the RE element together with the Al. These comments notwithstanding, it is hereby acknowledged that the etching process is much more complicated than simply breaking bonds and what is presented is at best a comparison of the RE-*i*-MAX systems with respect to previous reports for regular *i*-MAX phases [38,52].

D. Exfoliation energy

The second criterion used to determine whether a RE-*i*-MAX phase could be successfully etched is its exfoliation energy [49]. The exfoliation energy E_{exf} can be evaluated as

$$E_{exf} = -[E_{tot}(\text{RE-}i\text{-MAX}) - 2E_{tot}(\text{RE-}i\text{-MXene}) - 12E_{tot}(\text{Al})]/(4S), \quad (10)$$

where $S = ab\sin(\beta\frac{\pi}{180})$ is the surface area and a, b, and β are the structural parameters listed in Table I. E_{tot}(RE-*i*-MAX), E_{tot}(RE-*i*-MXene), and E_{tot}(Al), respectively, correspond to the ground-state energy of RE-*i*-MAX, RE-*i*-MXene, and bulk aluminum per atom. E_{tot}(RE-*i*-MXene) was computed for the pristine MXene system with optimized atomic positions inside the cell. Since two RE-*i*-MXene sheets are produced from the etching of the parent RE-*i*-MAX phase, the total energy is divided by four times the surface area. The computed exfoliation energies of the various RE-*i*-MAX phases are listed in Table III.

TABLE III. Exfoliation energy E_{exf} (eV/Å^2) for nine different RE-*i*-MAX phases with RE = Nd, Sm, Gd, Tb, Dy, Ho, Er, Tm, and Lu, calculated using Eq. (10). For comparison, exfoliation energies of three conventional MAX phases are listed [49].

Compound	E_{exf} (eV/Å^2)
$(Mo_{2/3}Nd_{1/3})_2AlC$	0.126
$(Mo_{2/3}Sm_{1/3})_2AlC$	0.136
$(Mo_{2/3}Gd_{1/3})_2AlC$	0.143
$(Mo_{2/3}Tb_{1/3})_2AlC$	0.146
$(Mo_{2/3}Dy_{1/3})_2AlC$	0.148
$(Mo_{2/3}Ho_{1/3})_2AlC$	0.150
$(Mo_{2/3}Er_{1/3})_2AlC$	0.151
$(Mo_{2/3}Tm_{1/3})_2AlC$	0.153
$(Mo_{2/3}Lu_{1/3})_2AlC$	0.156
Ti_2AlC	0.164
Nb_2AlC	0.185
V_2AlC	0.205

Since no experimental exfoliation data can be found in the literature, the best we can do is compare these theoretical predictions to values for conventional MAX phases, reported by Khazaei *et al.* [49]. Among the successfully etched MAX phases, V_2AlC has the largest theoretical exfoliation energy of 0.205 eV/Å^2. Therefore, from the computed values in Table III, that are all smaller than the one of V_2AlC, we expect that RE-*i*-MAX phases could *a priori*, be successfully etched into RE-*i*-MXenes.

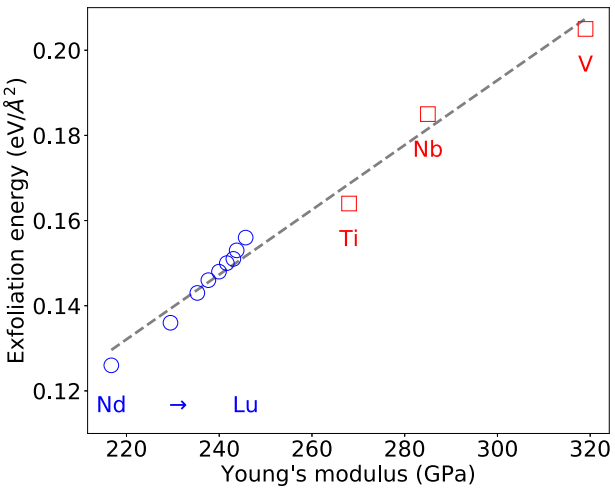

FIG. 7. Correlation between the computed Young's modulus (GPa) and calculated exfoliation energy (eV/Å^2), for the nine considered RE-*i*-MAX phases (blue circles). For comparison three conventional MAX phases, i.e., Ti_2AlC, Nb_2AlC, and V_2AlC [49,53], are also presented (red squares).

Combining the analysis of the bonding strength (Fig. 6) with the computed exfoliation energy in Table III, the exfoliation potential of RE-*i*-MAX phases is confirmed. Since no major difference is observed in the classification of the bonding strength for the various RE-*i*-MAX systems, the exfoliation energy values are used to sort the nine systems studied herein. The Nd-based compound is the most promising candidate for exfoliation, becuase the ease of exfoliation decreases with the RE atomic mass. This trend can be related to the values of the Young's moduli, as presented in Fig. 7. The larger the Young's modulus, the stiffer the system, and hence the larger the exfoliation energy. This is also consistent with the data reported for conventional MAX phases, i.e., Ti_2AlC, Nb_2AlC, V_2AlC [53], which all have Young's moduli that are larger than the one for the considered RE-*i*-MAX phases, and hence a larger exfoliation energy (see Fig. 7).

IV. CONCLUSION

In conclusion, this work not only addresses the electronic, elastic, and hardness properties of nine members of the rare-earth containing *i*-MAX single crystals—$(Mo_{2/3}RE_{1/3})_2AlC$, RE = Nd, Sm, Gd, Tb, Dy, Ho, Er, Tm, and Lu—but also sheds light on the exfoliation potential, via a complete analysis of both bond strengths and exfoliation energies. Similar to regular MAX phases, RE-*i*-MAX phases are quite stiff, with Young's moduli ranging from 215 to 245 GPa, as confirmed also by nanoindentation tests on a $(Mo_{2/3}Ho_{1/3})_2AlC$ single crystal. All bulk, shear, and Young's moduli increase with the mass of the RE element, which is consistent with the shrinking of the unit cell induced when moving from left to right on the lanthanide row. Considering that the theoretical values are obtained from first-principles calculations without taking either the temperature or the presence of defects into account, the agreement with the experimental values is remarkable.

The *ab initio* calculations of the electronic properties reveal the metallic character of all the systems under investigation and the complete analysis of the bonding strengths leads to the major conclusion that C-Mo and C-RE bonds are stronger than the Al-Mo and Al-RE ones. Finally, the computation of the exfoliation energy confirms the exfoliation potential of RE-*i*-MAX phases into RE-*i*-MXenes. The remaining challenge is to find an etching procedure strong enough to eliminate the aluminum planes while keeping the integrity of the 2D layers. We believe that this theoretical report on the exfoliation potential of RE-*i*-MAX phases represents a promising breakthrough for future experimental exfoliation of the presented nine RE-based systems, and their potential use in applications where 2D magnetic materials are desired.

ACKNOWLEDGMENTS

A.C., T.P., and J.-C.C. acknowledge financial support from the Fédération Wallonie-Bruxelles through the Action de Recherche Concertée (ARC) on 3D nanoarchitecturing of 2D crystals (No. 16/21-077), from the European Union's Horizon 2020 researchers and innovation program (Graphene Flagship Core 1 - No. 696656 and Core 2 - No. 785219), and from the Belgium FNRS. A.C. acknowledges the support of Wallonie-Bruxelles-International. LMGP was financially supported by the "Agence Nationale de la Recherche" (project ANR-18-CE09-0041). A.C., J.-C.C, and T.O. are also indebted to the Flag-ERA JTC 2017 project entitled "MORE-MXenes". M.W.B. acknowledges the financial support of the chair of excellence program of the Nanosciences Foundation (Université Grenoble-Alpes Foundation). Computational resources were provided by the supercomputing facilities of the UCLouvain (CISM) and the Consortium des Equipements de Calcul Intensif en Fédération Wallonie-Bruxelles (CECI) funded by the Fonds de la Recherche Scientifique de Belgique (F.R.S.- FNRS) under convention No. 2.5020.11. A.C. thanks J. George for her help in using the LOBSTER code, and H. Badr and M. Sokol from Drexel University for their time in teaching how to use the nanoindentor and the scanning electron microscope.

[1] M. W. Barsoum, Prog. Solid State Chem. **28**, 201 (2000).
[2] M. Sokol, V. Natu, S. Kota, and M. W. Barsoum, Trends Chem. **1**, 210 (2019), Special Issue Part Two: Big Questions in Chemistry.
[3] M. W. Barsoum, *MAX Phases*, 1st ed. (Wiley-Blackwell, London, 2013).
[4] M. W. Barsoum and T. El-Raghy, Am. Sci. **89**, 334 (2001).
[5] M. Nelson, M. T. Agne, B. Anasori, J. Yang, and M. W. Barsoum, Mater. Sci. Eng. A **705**, 182 (2017).
[6] M. Barsoum and G. Tucker, Scr. Mater. **139**, 166 (2017).
[7] M. W. Barsoum, X. Zhao, S. Shanazarov, A. Romanchuk, S. Koumlis, S. J. Pagano, L. Lamberson, and G. J. Tucker, Phys. Rev. Mater. **3**, 013602 (2019).
[8] M. Naguib, M. Kurtoglu, V. Presser, J. Lu, J. Niu, M. Heon, L. Hultman, Y. Gogotsi, and M. W. Barsoum, Adv. Mater. **23**, 4248 (2011).
[9] L. Verger, C. Xu, V. Natu, H.-M. Cheng, W. Ren, and M. W. Barsoum, Curr. Opin. Solid State Mater. Sci. **23**, 149 (2019).
[10] Y. Gogotsi and B. Anasori, ACS Nano **13**, 8491 (2019).
[11] M. Khazaei, A. Mishra, N. S. Venkataramanan, A. K. Singh, and S. Yunoki, Curr. Opin. Solid State Mater. Sci. **23**, 164 (2019).
[12] T. Cabioch, P. Eklund, V. Mauchamp, M. Jaouen, and M. W. Barsoum, J. Eur. Ceram. Soc. **33**, 897 (2013).
[13] F. Meng, Y. Zhou, and J. Wang, Scr. Mater. **53**, 1369 (2005).
[14] A. Mockute, J. Lu, E. J. Moon, M. Yan, B. Anasori, S. J. May, M. W. Barsoum, and J. Rosen, Mater. Res. Lett. **3**, 16 (2015).
[15] Z. Liu, E. Wu, J. Wang, Y. Qian, H. Xiang, X. Li, Q. Jin, G. Sun, X. Chen, J. Wang, and M. Li, Acta Mater. **73**, 186 (2014).
[16] Q. Tao, M. Dahlqvist, J. Lu, S. Kota, R. Meshkian, J. Halim, J. Palisaitis, L. Hultman, M. W. Barsoum, P. O. A. Persson, and J. Rosen, Nat. Commun. **8**, 1 (2017).
[17] M. Dahlqvist, J. Lu, R. Meshkian, Q. Tao, L. Hultman, and J. Rosen, Sci. Adv. **3**, e1700642 (2017).
[18] Q. Tao, J. Lu, M. Dahlqvist, A. Mockute, S. Calder, A. Petruhins, R. Meshkian, O. Rivin, D. Potashnikov, E. Caspi, H.

Shaked, A. Hoser, C. Opagiste, R.-M. Galera, R. Salikhov, U. Wiedwald, C. Ritter, A. R. Wildes, B. Johansson, L. Hultman, M. Farle, M. W. Barsoum, and J. Rosen, Chem. Mater. **31**, 2476 (2019).
[19] A. Petruhins, J. Lu, L. Hultman, and J. Rosen, Mater. Res. Lett. **7**, 446 (2019).
[20] P. Hohenberg and W. Kohn, Phys. Rev. **136**, B864 (1964).
[21] W. Kohn and L. J. Sham, Phys. Rev. **140**, A1133 (1965).
[22] G. Kresse and J. Hafner, Phys. Rev. B **47**, 558 (1993).
[23] G. Kresse and J. Furthmüller, Comput. Mater. Sci. **6**, 15 (1996).
[24] G. Kresse and J. Furthmüller, Phys. Rev. B **54**, 11169 (1996).
[25] J. P. Perdew, K. Burke, and M. Ernzerhof, Phys. Rev. Lett. **77**, 3865 (1996).
[26] J. Sun, A. Ruzsinszky, and J. P. Perdew, Phys. Rev. Lett. **115**, 036402 (2015).
[27] J. Sun, R. C. Remsing, Y. Zhang, Z. Sun, A. Ruzsinszky, H. Peng, Z. Yang, A. Paul, U. Waghmare, X. Wu, M. L. Klein, and J. P. Perdew, Nat. Chem. **8**, 831 (2016).
[28] P. E. Blöchl, Phys. Rev. B **50**, 17953 (1994).
[29] G. Kresse and D. Joubert, Phys. Rev. B **59**, 1758 (1999).
[30] A. Champagne, O. Chaix-Pluchery, T. Ouisse, D. Pinek, I. Gélard, L. Jouffret, M. Barbier, F. Wilhelm, Q. Tao, J. Lu, J. Rosen, M. W. Barsoum, and J.-C. Charlier, Phys. Rev. Mater. **3**, 053609 (2019).
[31] H. J. Monkhorst and J. D. Pack, Phys. Rev. B **13**, 5188 (1976).
[32] R. Dronskowski and P. E. Bloechl, J. Phys. Chem. **97**, 8617 (1993).
[33] V. L. Deringer, A. L. Tchougréeff, and R. Dronskowski, J. Phys. Chem. A **115**, 5461 (2011).
[34] S. Maintz, V. L. Deringer, A. L. Tchougréeff, and R. Dronskowski, J. Comput. Chem. **34**, 2557 (2013).
[35] S. Maintz, V. L. Deringer, A. L. Tchougréeff, and R. Dronskowski, J. Comput. Chem. **37**, 1030 (2016).
[36] Y. Le Page and P. Saxe, Phys. Rev. B **65**, 104104 (2002).
[37] K. Momma and F. Izumi, J. Appl. Crystallogr. **44**, 1272 (2011).
[38] R. Meshkian, M. Dahlqvist, J. Lu, B. Wickman, J. Halim, J. Thörnberg, Q. Tao, S. Li, S. Intikhab, J. Snyder, M. W. Barsoum, M. Yildizhan, J. Palisaitis, L. Hultman, P. O. A. Persson, and J. Rosen, Adv. Mater. **30**, 1706409 (2018).
[39] Z.-J. Wu, E.-J. Zhao, H.-p. Xiang, X.-f. Hao, X.-j. Liu, and J. Meng, Phys. Rev. B **76**, 054115 (2007).
[40] F. Mouhat and F.-X. Coudert, Phys. Rev. B **90**, 224104 (2014).
[41] R. Hill, Proc. Phys. Soc. A **65**, 349 (1952).
[42] M. Dahlqvist, A. Thore, and J. Rosen, J. Phys.: Condens. Matter **30**, 305502 (2018).
[43] H. Fu, D. Li, F. Peng, T. Gao, and X. Cheng, Comput. Mater. Sci. **44**, 774 (2008).
[44] J. F. Nye, *Physical Properties of Crystals: Their Representation by Tensors and Matrices* (Oxford University Press, Oxford, 1985).
[45] M. W. Barsoum and M. Radovic, Annu. Rev. Mater. Res. **41**, 195 (2011).
[46] W. Oliver and G. Pharr, J. Mater. Res. **7**, 1564 (1992).
[47] I. C. Albayrak, S. Basu, A. Sakulich, O. Yeheskel, and M. W. Barsoum, J. Am. Ceram. Soc. **93**, 2028 (2010).
[48] M. Khazaei, V. Wang, C. Sevik, A. Ranjbar, M. Arai, and S. Yunoki, Phys. Rev. Mater. **2**, 074002 (2018).
[49] M. Khazaei, A. Ranjbar, K. Esfarjani, D. Bogdanovski, R. Dronskowski, and S. Yunoki, Phys. Chem. Chem. Phys. **20**, 8579 (2018).
[50] M. Khazaei, J. Wang, M. Estili, A. Ranjbar, S. Suehara, M. Arai, K. Esfarjani, and S. Yunoki, Nanoscale **11**, 11305 (2019).
[51] M. Dahlqvist and J. Rosen, Phys. Chem. Chem. Phys. **17**, 31810 (2015).
[52] Q. Tao, M. Dahlqvist, J. Lu, S. Kota, R. Meshkian, J. Halim, J. Palisaitis, L. Hultman, M. W. Barsoum, P. O. A. Persson, and J. Rosen, Nat. Commun. **8**, 14949 (2017).
[53] M. F. Cover, O. Warschkow, M. M. M. Bilek, and D. R. McKenzie, J. Phys.: Condens. Matter **21**, 305403 (2009).